Research Article

Deep learning-based quantitative analysis of lignite-derived carbon structures and optimization of supercapacitor performance

Xiaokang An[1,2], Jiaxin Zhang[1,2], Shaoxiong Han[3], Yuhui Feng[1,2], Yajing Wang[1,2], Peixiang Shi[1,2*], Yongzhen Wang[1,2*]

[1]College of Materials Science and Engineering, Taiyuan University of Technology, Taiyuan 030024, Shanxi, China.

[2]Innovation Research Center for Materials Genetic Engineering of Taiyuan University of Technology, Taiyuan 030024, Shanxi, China.

[3]College of Electronic Information Engineering, Taiyuan University of Technology, Taiyuan 030024, Shanxi, China.

***Correspondence to:** Prof. Yongzhen Wang, Prof. Peixiang Shi, College of Materials Science and Engineering, Taiyuan University of Technology, Taiyuan 030024, Shanxi, China. E-mail: wangyongzhen@tyut.edu.cn; shipeixiang@tyut.edu.cn

Received: 28 June 2026 | Approved: 20 July 2026 | Online: 20 July 2026

Abstract

Carbon nanotubes (CNTs) are promising electrode materials for supercapacitors due to their high electrical conductivity and structural stability. However, two key challenges remain: the lack of reliable quantitative descriptors for CNTs microstructures from SEM images and the insufficient incorporation of microstructural information into structure-performance models. To address these challenges, a structure-performance analysis framework is proposed by integrating deep learning-based instance segmentation with

response surface methodology (RSM), with a focus on feasibility under limited data conditions. A Mask R-CNN model is employed to automatically identify and segment CNTs in SEM images, enabling extraction of the CNTs area fraction as a quantitative microstructural descriptor. Under a small-sample scenario, the extracted structural parameter is combined with pore structure characteristics to establish a response surface model. Despite the limited dataset, the model achieves a reasonable predictive consistency ($R^2 = 0.937$), indicating that meaningful structure-performance relationships can be constructed with constrained data. This study highlights a data-efficient strategy for microstructure quantification and modeling, providing a feasible pathway for linking SEM-derived features with electrochemical behavior when data availability is limited.

Keywords: Carbon nanotubes, supercapacitors, mask R-CNN, microstructure quantification, response surface methodology

INTRODUCTION

Carbon nanotubes (CNTs), as a typical class of one-dimensional nanomaterials[1,2], have attracted widespread attention due to their excellent electrical conductivity, mechanical strength, and chemical stability[3-6]. Owing to these unique advantages, CNTs have demonstrated great potential across various fields, particularly in energy storage systems, where they have been extensively studied and applied[7-12]. Among these applications, CNTs exhibit notable structural and functional advantages in supercapacitors. Their unique hollow tubular structure not only facilitates the construction of continuous conductive networks but also promotes efficient electron transport within electrode materials, thereby significantly enhancing the overall electrochemical performance[13-16]. Previous studies have shown that the macroscopic performance of CNTs-based materials is strongly dependent on their microstructural characteristics. Specifically, microstructural features such as the orientation, diameter, aggregation state, and network structure of CNTs can significantly influence the electrical conductivity and ion transport properties of the materials[17,18]. Although other carbon nanomaterials, such as graphene, graphene oxide, and metal-organic framework (MOF)-derived porous carbons, have also

demonstrated excellent electrochemical performance, CNTs were selected in this study because they constitute the dominant conductive phase in lignite-derived porous carbon composites. Their one-dimensional morphology enables the formation of continuous conductive pathways throughout the carbon matrix, making their spatial distribution one of the key factors governing electron transport and charge storage behavior. Therefore, quantitative characterization of CNTs microstructures provides the most direct and physically meaningful approach for understanding the structure-performance relationship within the investigated material system. Therefore, accurate and reliable quantitative characterization of CNTs microstructures is essential for understanding structure-performance relationships and guiding electrode design. SEM is widely used for characterizing CNTs microstructures and provides direct morphological information at the nanoscale[19]. However, the analysis of SEM images in most studies still relies on manual observation, which is inefficient and lacks reproducibility[20,21].

This limitation becomes more pronounced when CNTs are intertwined with amorphous carbon and exhibit complex morphologies, making accurate quantitative analysis difficult. Therefore, automated and reliable microstructural analysis methods are urgently required. In recent years, deep learning has emerged as an effective approach for image segmentation tasks[22-24]. However, most existing methods are based on semantic segmentation, which can only provide category-level information and lacks the ability to distinguish individual instances.

In contrast, Mask R-CNN enables instance-level segmentation, making it particularly suitable for identifying overlapping and intertwined CNTs structures in SEM images. This capability allows for more accurate quantitative analysis of individual CNTs. RSM is widely used for modeling and optimizing material performance[25-27]. However, most existing models rely primarily on experimental conditions or process parameters, with limited consideration of microstructural characteristics.

Despite these advances, two key challenges remain: the lack of reliable quantitative descriptors for CNTs microstructures from SEM images and the limited incorporation of such information in structure-performance models[28,29]. To address this, a framework integrating instance-level deep learning segmentation with response surface modeling is proposed. Mask R-CNN is employed to resolve overlapping CNTs and extract the CNTs area fraction, which is adopted as the representative microstructural descriptor in this work. Compared with descriptors such as CNTs length, orientation, or curvature, the area fraction can be extracted more robustly and reproducibly from SEM images while remaining directly related to the density and continuity of conductive networks. As the CNTs area fraction increases, interconnected conductive pathways are progressively established, facilitating electron transport; however, excessive CNTs accumulation may also induce aggregation and partially block pore channels, thereby affecting ion transport. Therefore, the CNTs area fraction provides a physically meaningful bridge between SEM-observed microstructures and electrochemical performance.

The proposed framework enables automated and high-throughput microstructural quantification while establishing an interpretable connection between microstructure and electrochemical performance. Unlike conventional machine learning models that primarily employ synthesis parameters or material compositions as input variables, the present framework directly transforms SEM-derived microstructural information into quantitative descriptors and incorporates them into the response surface model. Consequently, the developed model is capable of capturing not only statistical correlations but also physically meaningful structure-performance relationships. Although demonstrated using lignite-derived CNTs/porous carbon composites, the proposed workflow can be readily extended to other porous carbon materials and microstructure-driven materials informatics studies.

MATERIALS AND METHODS

Material preparation and SEM imaging

Lignite-derived CNTs/porous carbon composite materials were synthesized via chemical activation. Lignite and K_2CO_3 were mixed at different mass ratios, followed by ball milling and high-temperature pyrolysis under a nitrogen atmosphere. The resulting products were washed and dried to obtain the final materials. SEM was employed to characterize the microstructure of the composites. Detailed information regarding preparation conditions is provided in the Supporting Information.

Dataset annotation and preprocessing

Three morphological categories were defined for annotation: amorphous carbon (C), carbonaceous particles (DKT), and carbon nanotubes (CNTs). All SEM images were annotated using the LabelMe tool and subsequently converted into COCO format. The dataset was randomly split into training (80%) and validation (20%) sets. To improve model generalization, data augmentation techniques—including random flipping, rotation, and scaling—were applied. Further details on the annotated dataset and representative images are available in the Supporting Information [Supplementary Figures 1 and 2].

Mask R-CNN model construction and training

A Mask R-CNN framework with a ResNet-50 + Feature Pyramid Network (FPN) backbone was adopted for instance segmentation of CNTs in SEM images[30-32]. Compared with semantic segmentation methods, Mask R-CNN enables instance-level discrimination, which is critical for resolving overlapping and entangled CNTs structures. Transfer learning was employed using weights pretrained on ImageNet[33]. To enhance the segmentation of slender CNTs structures, a dynamic loss weighting strategy was applied: the classification and mask losses were multiplied by a factor of 1.5 during the initial training phase, and then restored to default ratios as training progressed[34-37]. The model was trained for 200 epochs. Detailed descriptions of the model architecture, training parameters, and hyperparameter settings are provided in the Supporting Information [Figures 1 and 2].

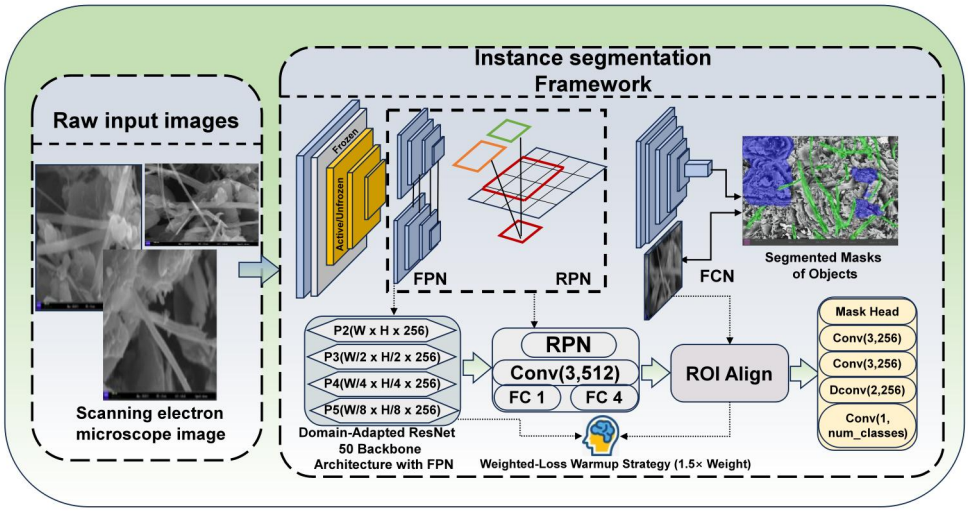

Figure 1. Architecture of the Mask R-CNN framework. FPN, Feature Pyramid Network; RPN, Region Proposal Network; FCN, Fully Convolutional Network; ROI, Region of Interest; FC, Fully Connected; Conv, Convolution.

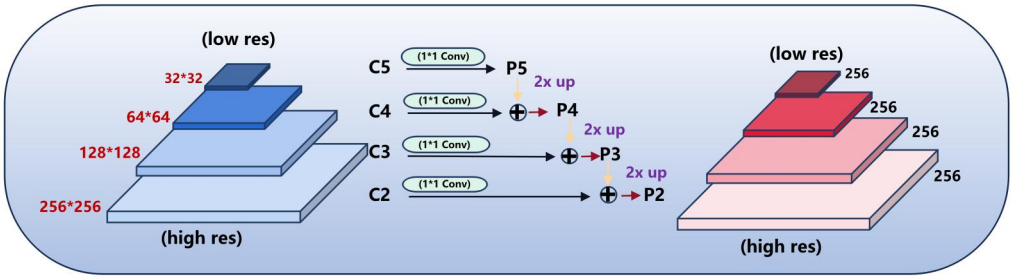

Figure 2. Feature Pyramid Network architecture. res, resolution; up, upsampling.

Quantitative microstructural analysis

Following instance segmentation, the CNTs area fraction was calculated as the ratio of the total pixel area occupied by CNTs to the entire SEM image area. This parameter was selected as the primary microstructural descriptor because it provides a direct quantitative representation of conductive network formation while remaining robust under limited image resolution and small-sample conditions.

Compared with descriptors such as CNTs length, orientation, or curvature, which require high-resolution imaging and complicated post-processing algorithms, the area fraction

can be extracted automatically and reproducibly from standard SEM images. Moreover, the CNTs area fraction reflects both the abundance and spatial continuity of conductive pathways within the porous carbon matrix. A moderate increase in CNTs area fraction generally facilitates electron transport by improving conductive network connectivity, whereas excessive CNTs accumulation may cause aggregation, reduce pore accessibility, and hinder electrolyte diffusion. Therefore, the CNTs area fraction provides a physically meaningful descriptor for linking microstructural characteristics with electrochemical performance.

Data collection and reliability for performance modeling

To ensure reliable correspondence between microstructure and electrochemical performance, SEM characterization, BET analysis, and electrochemical measurements were conducted using specimens prepared from the same synthesis batch. For each sample, multiple SEM images were collected from different regions to minimize the influence of local microstructural heterogeneity. The CNTs area fraction used for response surface modeling was obtained by averaging the segmentation results from these representative images.

Electrochemical measurements were repeated under identical testing conditions to verify data reproducibility. Although the overall dataset remains relatively limited because of the time-consuming material preparation and electrochemical characterization procedures, each data point was experimentally validated and reflects physically meaningful trends. Consequently, the dataset provides a reliable basis for establishing a preliminary structure-performance relationship under small-sample conditions.

Response surface modeling (RSM)

The CNTs area fraction, together with key experimental factors (e.g., activator ratio, micropore surface area, mesopore surface area), was incorporated into a quadratic response surface model to predict the specific capacitance of the supercapacitors. The

model was constructed based on experimentally measured data and microstructural parameters. Model fitting, analysis of variance (ANOVA), and three-dimensional response surface plots were generated to evaluate the influence of microstructural and processing parameters on performance[25,38].

RESULTS AND DISCUSSION

Training process analysis

The model was trained for 200 epochs. In the early stages, the classification and mask segmentation losses were multiplied by a factor of 1.5 to speed up convergence and ensure these branches learned effectively. This encouraged the model to establish reliable class discrimination and accurate target region segmentation, which in turn supported better bounding box regression and overall detection performance in later stages. As training progressed and the model began to converge, the loss weights were returned to their default values, allowing balanced optimization across all branches.

The total loss for each epoch was recorded automatically, and the training loss curve is shown in Figure 3, which illustrates a rapid decrease in the early stage and stable behavior in the middle and late stages with no significant fluctuations. The results indicate that the learning rate schedule and optimization strategy were properly configured and that the training process remained stable throughout.

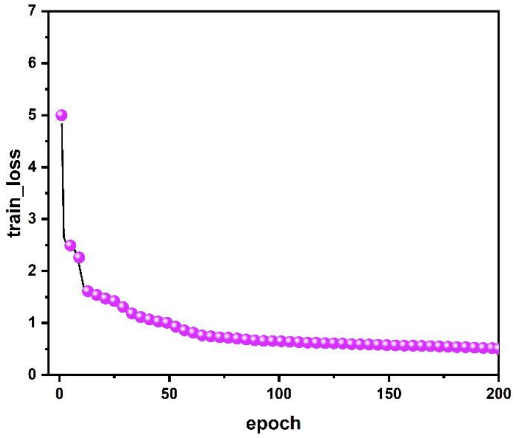

Figure 3. Training loss curve of the model.

Evaluation of object detection and segmentation performance

To evaluate convergence and detection performance during training, key metrics—including mIoU, F1-score, recall, precision, AP50, and overall AP—were tracked over all epochs[39], as shown in Figure 4. Most metrics increased rapidly in the early stages and gradually stabilized, indicating that the model achieves effective convergence within relatively few epochs.

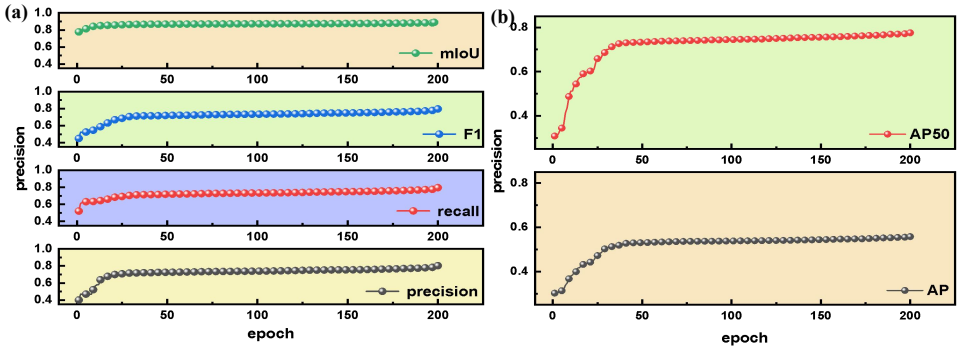

Figure 4. Training convergence curves of the model: (a) Training curves of mIoU, F1-score, Recall, and Precision; (b) Curves of AP50 and overall AP for the model.

AP50 improved significantly during the first few epochs and largely stabilized around the 40th epoch, suggesting that reliable object localization is established early. The overall AP followed a similar trend but increased more gradually, reflecting stable detection under stricter IoU thresholds. Precision rose quickly at the beginning and then plateaued, while recall continued to improve, and the F1-score gradually stabilized, demonstrating a balanced trade-off between detection accuracy and completeness.

For instance segmentation, mIoU increased steadily and reached a plateau, indicating that the model progressively learns more accurate object boundaries in the mask prediction task. By the end of training, the model achieved an AP50 of 0.8, overall AP of 0.6, and a final mIoU of 0.9, confirming its effectiveness in both object detection and instance segmentation of CNTs structures. Overall, the trends shown in Figure 4 indicate favorable

convergence characteristics and consistently stable performance across all evaluated metrics.

Prediction residuals and classification performance analysis

To evaluate the model's performance in classification and object localization, an error analysis of the detection results was conducted, as shown in Figure 5, including the confusion matrix, distribution of bounding box regression residuals, and cumulative distribution curve of IoU.

In terms of object localization error analysis, the center offsets (dx, dy) and scale residuals (dw, dh) of the predicted bounding boxes relative to the ground-truth annotations were statistically evaluated. As shown in the residual distribution histograms [Figure 5 a, d], the center offsets of most predicted bounding boxes are concentrated near zero, indicating that the deviation between the predicted box centers and the true object centers is generally small. The scatter distribution results [Figure 5 b, e] further demonstrate that the majority of samples cluster around the origin region, suggesting that the model exhibits good stability in object localization. Additionally, the scale residual distribution presents a relatively symmetric pattern without significant systematic bias, indicating that the model demonstrates reliable performance in bounding box scale regression.

As shown in the confusion matrix [Figure 5 c], the prediction results for most samples are concentrated along the diagonal, indicating that the model exhibits good recognition capability for the main categories. Specifically, 50 amorphous carbon (C) samples were correctly identified, and 30 CNTs samples were correctly classified, demonstrating that the model can accurately distinguish between different types of target structures in most cases. Meanwhile, a certain degree of misclassification still exists in a small number of samples, with some instances being misidentified as adjacent categories. This may be attributed to the similar textural features and morphological structures among different phases in CNTs microscopy images.

To more intuitively quantify the distribution proportion of localization errors, the cumulative probability distribution curves of the residuals were further analyzed [Figure 5 f]. It can be observed from the figure that the red curves representing center offsets (dx, dy) are steeper and closer to the vertical axis compared to the black curves representing scale residuals (dw, dh). The model demonstrates higher accuracy in center localization compared to scale regression. Specifically, approximately 80% of the samples have center offset residuals controlled within 0.15, and when the residual threshold reaches 0.22, the cumulative probability exceeds 0.9. This means that over 90% of the predicted bounding boxes achieve highly accurate localization, demonstrating the model's strong regression stability and robustness in detecting nanoscale targets against complex backgrounds.

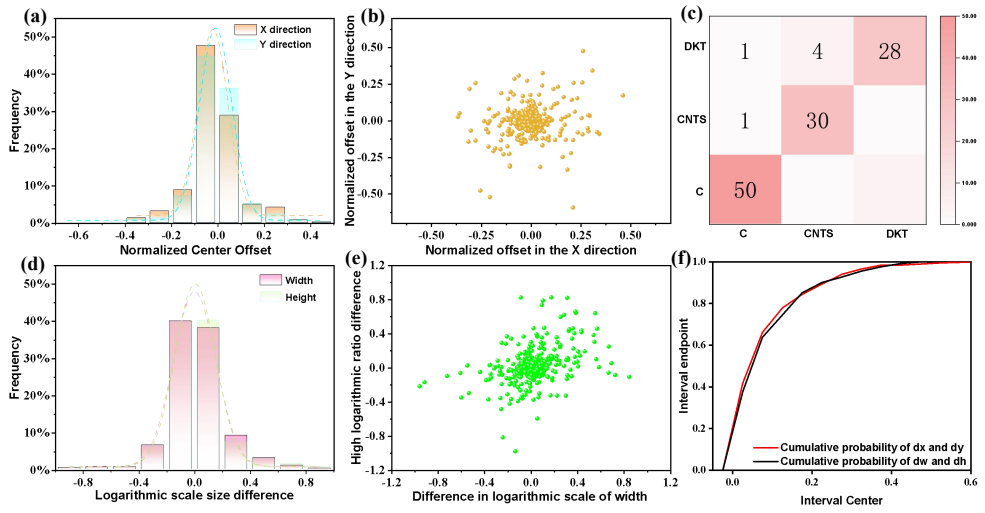

Figure 5. Error analysis of model detection: (a) Residual histograms of dx and dy; (b) Scatter plots of dx and dy offsets; (c) Confusion matrix for model classification; (d) Residual histograms of dw and dh; (e) Scatter plots of dw and dh scale residuals; (f) Cumulative residual curves

Visualization analysis and discussion

In this study, multiple representative CNTs microscopy images were selected to conduct a comparative experiment on the impact of the 1.5 × dynamic weighting strategy on

microscopic image segmentation performance. Model predictions were performed under two conditions—standard weighting (1.0) and improved weighting (1.5) and the segmentation results were analyzed visually to intuitively evaluate the effect of weight adjustment on the model's segmentation capability.

Under the 1.5 × dynamic weighting strategy, the model demonstrates improved segmentation performance for CNTs microscopy images, particularly in terms of boundary continuity and instance separation in dense CNTs regions. As shown in Figure 6, the improved model better preserves the elongated structural features of CNTs. In the terminal regions of CNTs, the segmentation results better maintain fiber continuity, with noticeably reduced truncation at the ends. In complex areas where multiple CNTs intersect or overlap, the model still clearly distinguishes the structural boundaries of individual instances, achieving relatively accurate instance separation. This indicates that the dynamic weighting strategy strengthens the segmentation branch's attention to CNTs boundaries and detailed features, thereby improving the recognition capability for complex microstructures. In addition, in high-density CNTs regions, the predicted masks are more continuous and structurally complete overall, providing a more reliable data foundation for subsequent CNTs area proportion calculation and structural statistical analysis.

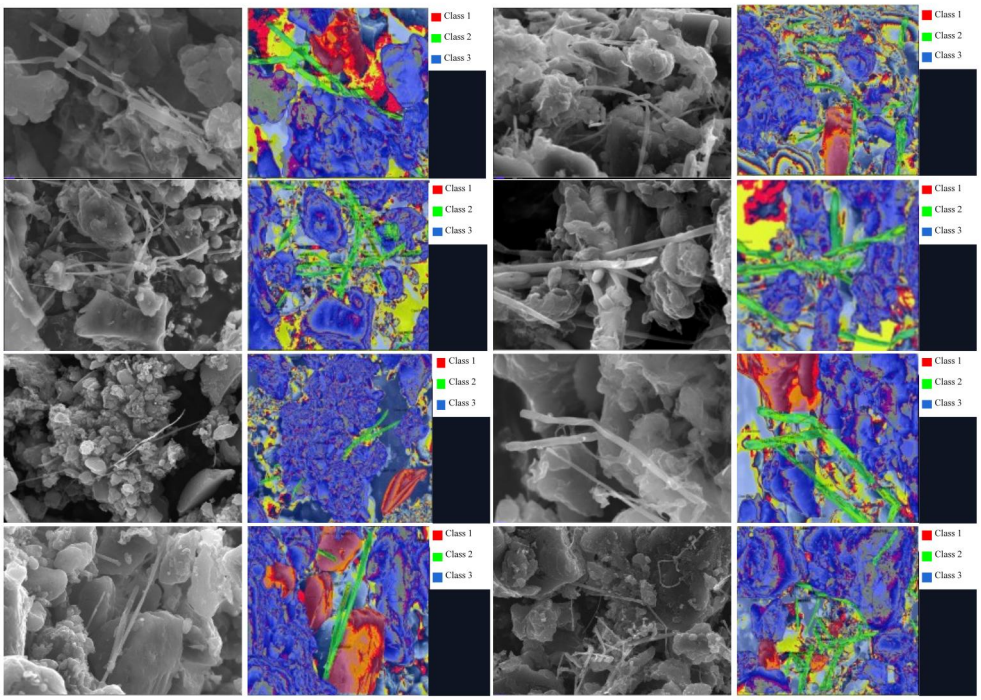

Figure 6. Segmentation results of the model under the 1.5 × weighting strategy.

Figure 7 presents the segmentation results of CNTs microscopy images under the standard weighting condition (1.0), aiming to validate the effectiveness of the dynamic weighting strategy. In comparison with Figure 6, the segmentation results under standard weighting exhibit certain limitations in regions with complex structures. Due to the characteristic crossing, intertwining, and high-density distribution of CNTs in microscopy images, the model shows edge truncation, structural fractures, and missed detections in some areas. Particularly at the terminal regions of CNTs and in areas where multiple nanotubes intersect, partial structures cannot be completely identified, leading to adhesion or structural blurring in the predicted masks. These issues indicate that under standard weighting conditions, the segmentation branch pays insufficient attention to the elongated structure of CNTs, thereby affecting the model's segmentation accuracy in complex microstructure scenarios.

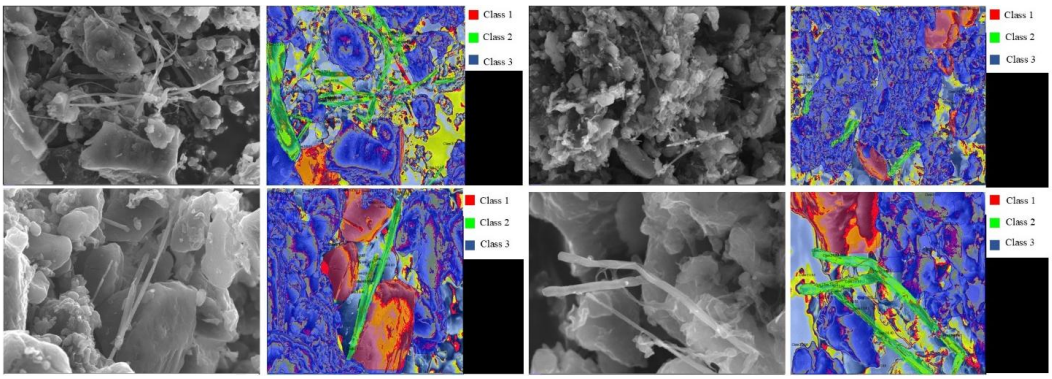

Figure 7. Segmentation results of the model under the standard weighting strategy.

Through comparative analysis, the dynamic loss-weighting strategy noticeably improves the segmentation performance for complex CNTs microstructures. Increasing the weights of the classification and mask branches during the early training stage enables the network to place greater emphasis on learning discriminative boundary information and fine structural details before the localization branch becomes dominant. This strategy is particularly beneficial for CNTs microscopy images because CNTs generally exhibit elongated morphologies, large aspect ratios, frequent overlap, and blurred boundaries.

The improved segmentation quality is reflected not only by the preservation of continuous CNTs structures but also by the enhanced separation of adjacent nanotubes in densely interconnected regions. Accurate identification of these individual CNTs instances is essential for subsequent quantitative analysis because under-segmentation may underestimate the conductive network density, whereas over-segmentation may artificially increase the calculated CNTs area fraction. Both situations would directly affect the reliability of the subsequent structure-performance model.

More importantly, accurate instance segmentation provides a reliable foundation for microstructural quantification. Since the CNTs area fraction serves as the key structural descriptor in the response surface model, improvements in segmentation accuracy directly reduce the uncertainty of structural parameter extraction. Therefore, the dynamic weighting strategy contributes not only to better image segmentation performance but

also to the robustness and physical reliability of the subsequent electrochemical performance prediction.

Response surface analysis

Response surface model establishment and analysis of variance

After obtaining the instance segmentation results, the pixel-wise areas of CNTs regions were quantified based on the predicted masks, and the corresponding area fractions of CNTs in the SEM images were calculated. By statistically analyzing multiple SEM images for each sample, the CNTs area fractions, together with the corresponding synthesis parameters and electrochemical performance data, were obtained and organized as summarized in Table 1. Although the dataset size remains relatively limited due to the experimental complexity and the high cost of electrochemical measurements, it still contains sufficient and physically meaningful information for establishing a preliminary structure-performance relationship model. The activator ratio refers to the mass ratio between potassium carbonate (K_2CO_3) and lignite used during the activation process.

Table 1. CNTs area proportion and corresponding process parameters and performance data of the samples [Supplementary Figure 3].

Run	Activator ratio	Micropore surface area (m^2/g)	Mesopore surface area (m^2/g)	CNTs proportion (%)	Specific capacitance (F/g)
1	0	51	43	0	124
2	0.25	389	21	0	140
3	0.5	1,046	90	0.15	275
4	0.75	1,154	129	0.08	231
5	1	1,248	138	0.35	249
6	1.5	1,025	126	0.25	293
7	2	1,207	162	0.20	252
8	3	1,164	153	0.45	235

9	4	1,005	127	0.20	297

These results indicate notable variations in CNTs distribution density among samples, reflecting microstructural changes. The quantified CNTs area fraction exhibits substantial variation among different samples, indicating that the conductive network evolves significantly with synthesis conditions. This parameter was selected as the representative structural descriptor because it simultaneously reflects the abundance and spatial continuity of conductive CNTs pathways observed in SEM images. Compared with purely geometrical descriptors such as CNTs length or orientation, the area fraction can be extracted automatically with higher reproducibility while maintaining direct physical relevance to electron transport within porous electrodes.

From an electrochemical perspective, the conductive CNTs network functions as the primary pathway for electron transport during charge and discharge processes. When the CNTs area fraction is relatively low, conductive pathways remain discontinuous, resulting in increased internal resistance and reduced utilization of electrochemically active sites. As the CNTs area fraction increases, interconnected conductive networks become progressively established, facilitating electron transport and reducing charge-transfer resistance, thereby improving specific capacitance. However, excessive CNTs accumulation may cause local aggregation and partial blockage of pore channels, limiting electrolyte penetration into the porous structure and reducing ion transport efficiency. Consequently, an optimal CNTs area fraction is expected rather than a monotonic increase. To investigate the intrinsic relationships between various factors and the response values, response surface methodology was applied to analyze the experimental data using Design-Expert software, and a reduced quadratic model was established[25]. The results of analysis of variance and the predictive capability indicators are presented in Table 2 and Table 3, respectively.

Table 2. Analysis of variance (ANOVA) for the regression model.

Source	Sum of Squares	df	Mean Square	*F*-value	*P*-value
Model	0.0462	3	0.0154	24.90	0.0020
B	0.0013	1	0.0013	2.12	0.2054
D	0.0014	1	0.0014	2.24	0.1944
D^2	0.0071	1	0.0071	11.48	0.0195
Residual	0.0093	5	0.0019		
Total	0.0555	8			

Table 3. Goodness-of-fit and predictive capability statistical indicators for the reduced quadratic model.

Model statistics	R^2	Adjusted R^2	Predicted R^2	CV (%)	Adeq Precision
	0.9373	0.8996	0.7102	1.84	12.01

The significance and reliability of the model were evaluated through analysis of variance. The results indicate that the model has an *F*-value of 24.90 with a corresponding *p*-value of 0.002 ($p < 0.05$), demonstrating that the established regression model is statistically significant and capable of effectively describing the relationship between the experimental factors and the response values.

Based on the significance of the regression coefficients, the quadratic term D^2 exhibits a *p*-value of 0.0195 ($p < 0.05$), indicating that this quadratic term has a significant effect on the response value and serves as an important factor influencing the response variation in the system. In contrast, the linear terms of B (micropore surface area) and D (CNTs area proportion) do not reach the significance level, suggesting that their direct linear effects on the response value are relatively weak.

In terms of model fitting capability, the coefficient of determination $R^2 = 0.9373$ indicates

that the model can explain 93.73% of the response variation, demonstrating a high degree of fit. Furthermore, the difference between the adjusted R^2 (0.8996) and the predicted R^2 (0.7102) is less than 0.2, indicating that the model possesses good stability and predictive capability.

Furthermore, the coefficient of variation (CV) for the model is 1.84%, a relatively low value indicating good repeatability and reliability of the experimental data. The adequate precision value of 12.01 is substantially higher than the threshold value of 4, demonstrating that the model possesses a high signal-to-noise ratio and can provide a reliable basis for subsequent prediction and optimization of response values. Based on the regression analysis, the quadratic equation of the model is obtained as follows:

$$log_{10}(R)=2.10522+0.0001*B+1.75336*D-3.34395*D^2 \quad (1)$$

Here, R represents the response value, specific capacitance (F/g); B denotes the micropore specific surface area (m^2/g); and D is the area proportion of CNTs in SEM images at 16,000× magnification (%).It can be observed from the equation that factor D exhibits a significant quadratic effect on the response value. As D increases, the response value initially increases and then decreases, indicating the existence of an optimal level of this factor within the system.

Response surface and contour analysis

To further analyze the influence of micropore specific surface area (B) and CNTs proportion (D) on the response value, the corresponding three-dimensional response surface plot and contour plot were generated, as shown in Figure 8.

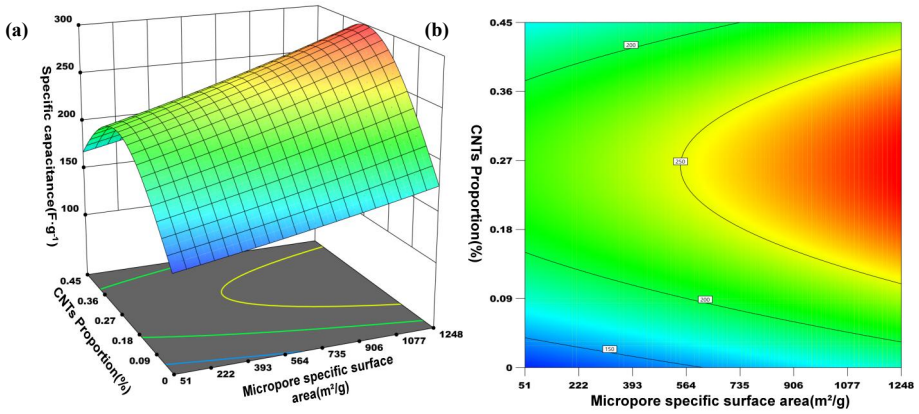

Figure 8. Visualization of the reduced quadratic model: (a) 3D response surface plot; (b) contour plot.

The three-dimensional response surface reveals a pronounced nonlinear dependence of specific capacitance on the CNTs area fraction (D), exhibiting an initial increase followed by a gradual decrease. This trend is consistent with the statistically significant quadratic term (D^2) in the regression model, indicating that the contribution of CNTs to electrochemical performance is governed by a balance between conductive network formation and pore accessibility rather than by a simple monotonic relationship.

At relatively low CNTs area fractions, the conductive pathways within the porous carbon matrix remain discontinuous, resulting in relatively high internal resistance and inefficient electron transport. Consequently, only a portion of the electrochemically active surface participates effectively in charge storage, leading to comparatively low specific capacitance. As the CNTs area fraction increases, individual nanotubes become progressively interconnected, forming a continuous conductive network that facilitates rapid electron transport and reduces charge-transfer resistance. Meanwhile, the interconnected CNTs framework also improves electrolyte penetration and ion diffusion by providing efficient transport pathways, thereby enhancing the utilization of active sites and increasing the specific capacitance[40,41].

However, when the CNTs area fraction exceeds the optimal range, excessive CNTs accumulation and local aggregation become increasingly significant. The overlap of

densely packed nanotubes may partially block micropores, reduce electrolyte accessibility, and increase ion diffusion resistance. Although electrical conductivity continues to improve, the restricted transport of electrolyte ions offsets this advantage, resulting in a gradual decline in capacitance. These results indicate that maximizing CNTs content alone is insufficient for achieving optimal electrochemical performance; instead, an appropriate balance between electronic conductivity and ionic transport must be established.

In contrast, the micropore specific surface area (B) exhibits a generally positive but comparatively weaker influence on capacitance, primarily by providing abundant electrochemically active sites for charge accumulation. The contour plot further shows only slight curvature, suggesting a relatively weak interaction between the microporous surface area and the CNTs area fraction. Consequently, the highest capacitance is achieved under conditions combining a high micropore surface area with a moderate CNTs area fraction, where conductive network continuity and pore accessibility are simultaneously optimized.

These observations further demonstrate that the CNTs area fraction is not merely a statistical fitting variable in the response surface model but a physically meaningful microstructural descriptor that quantitatively characterizes conductive network development. By incorporating SEM-derived quantitative microstructural information into the response surface model, the proposed framework establishes a more interpretable structure-performance relationship than conventional parameter-driven regression approaches, thereby providing a practical strategy for microstructure-guided optimization of porous carbon electrodes.

Additional diagnostic analysis was performed to further evaluate the reliability of the established response surface model. As shown in Supplementary Figure 4(a), the predicted values agree well with the experimental measurements and are closely

distributed around the diagonal line, demonstrating satisfactory predictive capability. Furthermore, the residuals are randomly distributed around zero without any obvious systematic trend [Supplementary Figure 4b], indicating that no significant model bias or heteroscedasticity is present and confirming the robustness of the established regression model.

Validation of model predictive performance

To further evaluate the predictive capability of the established response surface model, three new experimental conditions that were not involved in the model construction were selected for external validation after model fitting. The specific capacitance under these conditions was calculated using the response surface model, and the predicted values were compared with the corresponding experimental results. The CNTs area fractions of the three samples, determined from SEM images at a magnification of 1.6×10^4, were 0.13, 0.22, and 0.35, respectively. The corresponding identification results are shown in Figure 9.

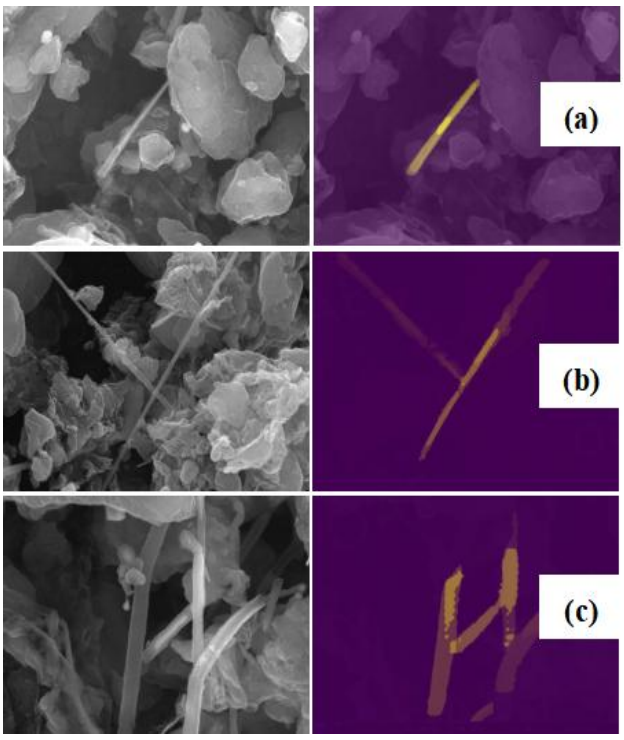

Figure 9. Identification results of the three samples from SEM images at a magnification of 1.6×10^4.

The micropore-specific surface area of each sample was obtained from BET measurements, and the corresponding parameters are summarized in Table 4.

Table 4. Micropore-specific surface area and CNTs fraction of each sample.

Sample ID	Micropore-specific surface area (m^2/g)	CNTs fraction (%)
a	1,190	0.13
b	1,050	0.22
c	1,280	0.35

In addition, the electrochemical performance of the samples was evaluated using a three-electrode system, and the comparison between the model-predicted and experimentally measured values is presented in Table 5.

Table 5. Comparison between experimental and predicted values for each sample.

Sample ID	Experimental value ($F \cdot g^{-1}$ (at 1 A g^{-1}))	Predicted value ($F \cdot g^{-1}$ (at 1 A g^{-1}))	Relative error (%)
a	160.6	140.7	12.4
b	300.4	281.2	6.4
c	240.9	276.1	14.6

The results indicate that the model predictions are in good overall agreement with the experimental measurements. The relative errors for the three samples are 12.4%, 6.4%, and 14.6%, respectively, all within 20%, demonstrating the satisfactory predictive accuracy of the established response surface model. Under varying CNTs fractions and pore structure parameters, the model is able to reliably capture the variation trend of the specific capacitance. These findings suggest that the model not only provides an effective fit to the existing experimental data but also possesses a certain level of predictive

capability.

A further analysis of the prediction errors reveals that the deviation slightly increases when the CNTs fraction is relatively high or when the pore structure parameters deviate from the optimal range. This behavior may be attributed to the heterogeneity of the material microstructure and the localized aggregation of CNTs, which can affect the ion transport pathways of the electrolyte to some extent. Nevertheless, the model still provides a reasonably accurate description of the relationship between structural parameters and electrochemical performance. Therefore, the established response surface model demonstrates promising potential for guiding the structural optimization and performance prediction of lignite-derived porous carbon/CNTs composites.

CONCLUSIONS

This work integrates Mask R-CNN-based microstructure extraction with response surface methodology (RSM) to establish a quantitative structure-performance relationship for lignite-derived CNTs/porous carbon composites. Reliable instance segmentation enables accurate extraction of the CNTs area fraction from SEM images, providing a physically meaningful descriptor for conductive network formation. The developed response surface model demonstrates satisfactory predictive performance under limited experimental data and reveals that electrochemical performance is governed by the synergistic effect of conductive network continuity and microporous structure. These results demonstrate the feasibility of incorporating SEM-derived microstructural descriptors into performance modeling, providing an interpretable strategy for microstructure-guided optimization of porous carbon electrodes. Future work will focus on incorporating additional microstructural descriptors, such as CNTs orientation, connectivity, and length distribution, together with larger datasets to further improve model accuracy and generalization capability.

DECLARATIONS

Authors' contributions

Writing-original draft: XK An;

Conceptualization: JX Zhang, SX Han;

Writing-review and editing: SX Han;

Validation and visualization: YH Feng;

Data curation and formal analysis: YJ Wang;

Supervision, project administration, manuscript revision: PX Shi;

Supervision, funding acquisition, project administration, manuscript revision: YZ Wang;

All authors read and approved the final manuscript.

Availability of data and materials

The data are reflected in the Supplementary Materials.

AI and AI-assisted tools statement

The authors used AI-assisted tools during manuscript preparation, including language refinement and partial code development assistance. All model design, experimental setup, data analysis, interpretation of results, and scientific conclusions were independently completed, reviewed, and verified by the authors. The authors take full responsibility for the content of the final manuscript.

Financial support and sponsorship

This work was supported by the National Natural Science Foundation of China General Program (Grant No.52371231), and “Double Hundred Tackling Action” Program of Taiyuan City (Grant No. 2025TYJB13)

Conflicts of interest

All authors declared that there are no conflicts of interest.

REFERENCES

[1] Smalley, R. E. Carbon nanotubes: synthesis, structure, properties, and applications. Springer: Berlin, 2003.[Corpus ID: 135785323]

[2] Itami, K.; Maekawa, T. Molecular Nanocarbon Science: Present and Future. *Nano Lett.* 2020, 20, 4718-20.[DOI: 10.1021/acs.nanolett.0c02143]

[3] Ali, Z.; Yaqoob, S.; Yu, J.; D'Amore, A. Critical review on the characterization, preparation, and enhanced mechanical, thermal, and electrical properties of carbon nanotubes and their hybrid filler polymer composites for various applications. *Compos. Part C Open Access* 2024, 13, 100434.[DOI: 10.1016/j.jcomc.2024.100434]

[4] De Volder, M. F.; Tawfick, S. H.; Baughman, R. H.; Hart, A. J. Carbon nanotubes: present and future commercial applications. *Science* 2013, 339, 535-9.[DOI:10.1126/science.1222453]

[5] Hughes, K. J.; Iyer, K. A.; Bird, R. E.; et al. Review of Carbon Nanotube Research and Development: Materials and Emerging Applications. *ACS Appl. Nano Mater.* 2024, 7, 18695-713.[DOI: 10.1021/acsanm.4c02721]

[6] Pan, H.; Li, J.; Feng, Y. P. Carbon Nanotubes for Supercapacitor. *Nanoscale Res Lett* 2010, 5, 654-68.[DOI: 10.1007/s11671-009-9508-2]

[7] Saito, R.; Dresselhaus, G.; Dresselhaus, M. Electronic structure of double-layer graphene tubules. *J. Appl. Phys.* 1993, 73, 494-500.[DOI: 10.1063/1.353358]

[8] Dresselhaus, M.; Dresselhaus, G.; Saito, R. C60-related tubules. *Solid State Commun.* 1992, 84, 201-25.[DOI: 10.1016/0038-1098(92)90325-4]

[9] Issi, J.-P.; Langer, L.; Heremans, J.; Olk, C. Electronic properties of carbon nanotubes: experimental results. *Carbon* 1995, 33, 941-8.[DOI: 10.1016/0008-6223(95)00023-7]

[10] Ebbesen, T.; Lezec, H.; Hiura, H.; Bennett, J.; Ghaemi, H.; Thio, T. Electrical conductivity of individual carbon nanotubes. *Nature* 1996, 382, 54-6.[DOI: 10.1038/382054a0]

[11] Lin, H.; Li, L.; Ren, J.; et al. Conducting polymer composite film incorporated with aligned carbon nanotubes for transparent, flexible and efficient supercapacitor. *Sci Rep* 2013, 3, 1353.[DOI: 10.1038/srep01353]

[12] Conway, B. E. Electrochemical Supercapacitors: Scientific Fundamentals and Technological Applications; Springer: New York, 2013.[Corpus ID: 106453444]

[13] Gupta, V.; Kumar, S. MnO_2/SWCNTs buckypaper for high performance

supercapacitors. *Journal of Energy Storage* 2019, 26, 100960.[DOI: 10.1016/j.est.2019.100960]

[14] Simon, P.; Gogotsi, Y. Materials for electrochemical capacitors. *Nature Materials* 2008, 7, 845-54.[DOI: 10.1038/nmat2297]

[15] Frackowiak, E.; Béguin, F. Carbon materials for the electrochemical storage of energy in capacitors. *Carbon* 2001, 39, 937-50.[DOI: 10.1016/S0008-6223(00)00183-4]

[16] Liu, H.; Wang, Y.; Lv, L.; Liu, X.; Wang, Z.; Liu, J. Oxygen-enriched hierarchical porous carbons derived from lignite for high-performance supercapacitors. *Energy* 2023, 269, 126707.[DOI: 10.1016/j.energy.2023.126707]

[17] Herrero-Latorre, C.; Álvarez-Méndez, J.; Barciela-García, J.; García-Martín, S.; Peña-Crecente, R. M. Characterization of carbon nanotubes and analytical methods for their determination in environmental and biological samples: A review. *Analytica Chimica Acta* 2015, 853, 77-94.[DOI: 10.1016/j.aca.2014.10.008]

[18] Fu, X.; Wang, J.; Ding, J.; Wu, H.; Dong, Y.; Fu, Y. Quantitative evaluation of carbon nanotube dispersion through scanning electron microscopy images. *Composites Science and Technology* 2013, 87, 170-3.[DOI: 10.1016/j.compscitech.2013.08.014]

[19] Sevilla, M.; Mokaya, R. Energy storage applications of activated carbons: supercapacitors and hydrogen storage. *Energy Environ. Sci.* 2014, 7, 1250-80.[DOI: 10.1039/C3EE43525C]

[20] Bihani, A.; Daigle, H.; Santos, J. E.; Landry, C.; Prodanović, M.; Milliken, K. MudrockNet: Semantic segmentation of mudrock SEM images through deep learning. *Computers & Geosciences* 2022, 158, 104952.[DOI: 10.1016/j.cageo.2021.104952]

[21] Liu, H.; Cui, Z.; Sun, Y.; et al. Synergistic design and synthesis of O, N Co-doped hierarchical porous carbon for enhanced supercapacitor performance. *Energy Materials* 2025, 5.[DOI: 10.20517/energymater.2024.101]

[22] Wang, X.; Su, H.; Li, N.; Chen, Y.; Yang, Y.; Meng, H. A Deep Learning Labeling Method for Material Microstructure Image Segmentation. *Processes* 2023, 11, 3272.[DOI: 10.3390/pr11123272]

[23] R. Girshick. Fast R-CNN. In *2015 IEEE International Conference on Computer*

Vision (ICCV); 2015, pp1440-8.[DOI: 10.1109/ICCV.2015.169]

[24] Wang, Y.; Bai, Y.; Wang, P.; Wang, W.; Zhu, M.; Luo, M. Physically synthesized data for deep learning-based visual scratch inspection of aerospace alloys with complex geometries. *Journal of Materials Informatics* 2026, 6, 13.[DOI: 10.20517/jmi.2025.74]

[25] Rodrigues, D. M.; Rodríguez, E. C. A.; Marins, F. A. S.; Oliveira, I. de; Silva, M. B.; Silva, A. F. da. An innovative DMAIC and response surface methodology framework for optimizing carbon xerogel synthesis in proton exchange membrane fuel cells. *Energy* 2025, 340, 139173.[DOI: 10.1016/j.energy.2025.139173]

[26] Liu, H.; Cui, Z.; Qiao, Z.; An, X.; Wang, Y. Machine learning-assisted prediction, screen, and interpretation of porous carbon materials for high-performance supercapacitors. *Journal of Materials Informatics* 2024, 4.[DOI: 10.20517/jmi.2024.29]

[27] Yuan, S.; Zhu, Z.; Lu, J.; Cai, L.; Sun, Q. Computer vision for efficient object detection and segmentation in molecular image analysis. *Journal of Materials Informatics* 2026, 6, 17.[DOI: 10.20517/jmi.2025.78]

[28] Wei, X.; Wang, C.; Liu, X.; et al. Application of deep learning for predicting carbon segregation in large-diameter continuously cast steel billets. *Journal of Materials Informatics* 2026, 6, 19.[DOI: 10.20517/jmi.2025.73]

[29] Xue, M.; Mei, Z.; Hu, C.; Tian, Z.; Ren, Y.; Liu, C. Machine learning-assisted design of carbon nanotube-based single-atom catalysts for hydrogen evolution reaction. *Journal of Materials Informatics* 2026, 6, 22.[DOI: 10.20517/jmi.2025.96]

[30] Ren, S.; He, K.; Girshick, R.; Sun, J. Faster R-CNN: Towards Real-Time Object Detection with Region Proposal Networks. *IEEE Transactions on Pattern Analysis and Machine Intelligence* 2017, 39, 1137-49.[DOI: 10.1109/TPAMI.2016.2577031]

[31] He, K.; Zhang, X.; Ren, S.; Sun, J. Deep Residual Learning for Image Recognition. In*2016 IEEE Conference on Computer Vision and Pattern Recognition (CVPR)*; 2016, 770-8.[DOI: 10.1109/CVPR.2016.90]

[32] Lin, T.-Y.; Dollar, P.; Girshick, R.; He, K.; Hariharan, B.; Belongie, S. Feature Pyramid Networks for Object Detection. In*2017 IEEE Conference on Computer Vision and Pattern Recognition (CVPR)*; IEEE, 2017, 936-44.[DOI: 10.1109/CVPR.2017.106]

[33] Yosinski, J.; Clune, J.; Bengio, Y.; Lipson, H. How transferable are features in deep neural networks?, 2014. *arXiv 2014*, arXiv:1411.1792.[DOI: 10.48550/arXiv.1411.1792]

[34] He, K.; Gkioxari, G.; Dollár, P.; Girshick, R. Mask R-CNN, 2018. arXiv 2018, arXiv:1703.06870.[DOI: 10.48550/arXiv.1703.06870]

[35] Terven, J.; Cordova-Esparza, D.-M.; Romero-González, J.-A.; Ramírez-Pedraza, A.; Chávez-Urbiola, E. A. A comprehensive survey of loss functions and metrics in deep learning. *Artif. Intell. Rev.* 2025, 58, 195.[DOI: 10.1007/s10462-025-11198-7]

[36] Loshchilov, I.; Hutter, F. SGDR: Stochastic Gradient Descent with Warm Restarts, 2017. *arXiv* 2017, arXiv.1608.03983.[DOI: 10.48550/arXiv.1608.03983]

[37] Micikevicius, P.; Narang, S.; Alben, J.; et al. Mixed Precision Training, 2018. *arXiv* 2018, arXiv.1710.03740.[DOI: 10.48550/arXiv.1710.03740]

[38] Li, C.; Han, X.; Yao, C.; Ban, X. MatSAM: Efficient Extraction of Microstructures of Materials via Visual Large Model, 2024. *arXiv* 2024, arXiv.2401.05638.[DOI: 10.48550/arXiv.2401.05638]

[39] Tharwat, A. Classification assessment methods. *ACI* 2021, 17, 168-92.[DOI: 10.1016/j.aci.2018.08.003]

[40] Zhong, J.; Yang, Z.; Mukherjee, R.; et al. Carbon nanotube sponges as conductive networks for supercapacitor devices. *Nano Energy* 2013, 2, 1025-30.[DOI: 10.1016/j.nanoen.2013.04.001]

[41] Fu, H.; Du, Z.; Zou, W.; Li, H.; Zhang, C. Carbon nanotube reinforced polypyrrole nanowire network as a high-performance supercapacitor electrode. *Journal of Materials Chemistry A* 2013, 1, 14943-50.[DOI: 10.1039/c3ta12844j]